Radon Removal in XENONnT down to the Solar Neutrino Level

E. Aprile [1], J. Aalbers [2], K. Abe [3], S. Ahmed Maouloud [4], L. Althueser [5], B. Andrieu [4], E. Angelino [6,7], D. Antón Martin [8], F. Arneodo [9], L. Baudis [10], M. Bazyk [11], L. Bellagamba [12], R. Biondi [13,14], A. Bismark [10], K. Boese [13], A. Brown [15], G. Bruno [11], R. Budnik [14], C. Cai [16], C. Capelli [10], J. M. R. Cardoso [17], A. P. Cimental Chávez [10], A. P. Colijn [18], J. Conrad [19], J. J. Cuenca-García [10], V. D'Andrea [7,*], L. C. Daniel Garcia [4], M. P. Decowski [18], A. Deisting [20], C. Di Donato [21,7], P. Di Gangi [12], S. Diglio [11], K. Eitel [22], S. el Morabit [18], A. Elykov [22], A. D. Ferella [21,7], C. Ferrari [7], H. Fischer [15], T. Flehmke [19], M. Flierman [18], W. Fulgione [6,7], C. Fuselli [18], P. Gaemers [18], R. Gaior [4], M. Galloway [10], F. Gao [16], S. Ghosh [23], R. Giacomobono [24], R. Glade-Beucke [15], L. Grandi [8], J. Grigat [15], H. Guan [23], M. Guida [13], P. Gyorgy [20], R. Hammann [13], A. Higuera [25], C. Hils [20], L. Hoetzsch [13], N. F. Hood [26], M. Iacovacci [24], Y. Itow [27], J. Jakob [5], F. Joerg [13,10,†], Y. Kaminaga [3], M. Kara [22], P. Kavrigin [14], S. Kazama [27], P. Kharbanda [18], M. Kobayashi [27], D. Koke [5], A. Kopec [26,‡], H. Landsman [14], R. F. Lang [23], L. Levinson [14], I. Li [25], S. Li [28], S. Liang [25], Z. Liang [28], Y.-T. Lin [13], S. Lindemann [15], M. Lindner [13], K. Liu [16], M. Liu [1,16], J. Loizeau [11], F. Lombardi [20], J. Long [8], J. A. M. Lopes [17,§], T. Luce [15], Y. Ma [26], C. Macolino [21,7], J. Mahlstedt [19], A. Mancuso [12], L. Manenti [9], F. Marignetti [24], T. Marrodán Undagoitia [13], K. Martens [3], J. Masbou [11], E. Masson [4], S. Mastroianni [24], A. Melchiorre [21,7], J. Merz [20], M. Messina [7], A. Michael [5], K. Miuchi [29], A. Molinario [6], S. Moriyama [3], K. Morå [1], Y. Mosbacher [14], M. Murra [1,5,¶], J. Müller [15], K. Ni [26], U. Oberlack [20], B. Paetsch [14], Y. Pan [4], Q. Pellegrini [4], R. Peres [10], C. Peters [25], J. Pienaar [8,14], M. Pierre [18], G. Plante [1], T. R. Pollmann [18], L. Principe [11], J. Qi [26], J. Qin [25], D. Ramírez García [10], M. Rajado [10], R. Singh [23], L. Sanchez [25], J. M. F. dos Santos [17], I. Sarnoff [9], G. Sartorelli [12], J. Schreiner [13], D. Schulte [5], P. Schulte [5], H. Schulze Eißing [5], M. Schumann [15], L. Scotto Lavina [4], M. Selvi [12], F. Semeria [12], P. Shagin [20], S. Shi [1], J. Shi [16], M. Silva [17], H. Simgen [13], C. Szyszka [20], A. Takeda [3], Y. Takeuchi [29], P.-L. Tan [19,1], D. Thers [11], F. Toschi [22], G. Trinchero [6], C. D. Tunnell [25], F. Tönnies [15], K. Valerius [22], S. Vecchi [30], S. Vetter [22], F. I. Villazon Solar [20], G. Volta [13], C. Weinheimer [5,**], M. Weiss [14], D. Wenz [5], C. Wittweg [10], V. H. S. Wu [22], Y. Xing [11], D. Xu [1], Z. Xu [1], M. Yamashita [3], L. Yang [26], J. Ye [31], L. Yuan [8], G. Zavattini [30], and M. Zhong [26]

(XENON Collaboration)[††]

[1] Physics Department, Columbia University, New York, NY 10027, USA
[2] Nikhef and the University of Groningen, Van Swinderen Institute, 9747AG Groningen, Netherlands
[3] Kamioka Observatory, Institute for Cosmic Ray Research, and Kavli Institute for the Physics and Mathematics of the Universe (WPI), University of Tokyo, Higashi-Mozumi, Kamioka, Hida, Gifu 506-1205, Japan
[4] LPNHE, Sorbonne Université, CNRS/IN2P3, 75005 Paris, France
[5] Institut für Kernphysik, University of Münster, 48149 Münster, Germany
[6] INAF-Astrophysical Observatory of Torino, Department of Physics, University of Torino and INFN-Torino, 10125 Torino, Italy
[7] INFN-Laboratori Nazionali del Gran Sasso and Gran Sasso Science Institute, 67100 L'Aquila, Italy
[8] Department of Physics, Enrico Fermi Institute & Kavli Institute for Cosmological Physics, University of Chicago, Chicago, IL 60637, USA
[9] New York University Abu Dhabi - Center for Astro, Particle and Planetary Physics, Abu Dhabi, United Arab Emirates
[10] Physik-Institut, University of Zürich, 8057 Zürich, Switzerland
[11] SUBATECH, IMT Atlantique, CNRS/IN2P3, Nantes Université, Nantes 44307, France
[12] Department of Physics and Astronomy, University of Bologna and INFN-Bologna, 40126 Bologna, Italy
[13] Max-Planck-Institut für Kernphysik, 69117 Heidelberg, Germany
[14] Department of Particle Physics and Astrophysics, Weizmann Institute of Science, Rehovot 7610001, Israel
[15] Physikalisches Institut, Universität Freiburg, 79104 Freiburg, Germany
[16] Department of Physics & Center for High Energy Physics, Tsinghua University, Beijing 100084, P.R. China
[17] LIBPhys, Department of Physics, University of Coimbra, 3004-516 Coimbra, Portugal
[18] Nikhef and the University of Amsterdam, Science Park, 1098XG Amsterdam, Netherlands
[19] Oskar Klein Centre, Department of Physics, Stockholm University, AlbaNova, Stockholm SE-10691, Sweden
[20] Institut für Physik & Exzellenzcluster PRISMA+, Johannes Gutenberg-Universität Mainz, 55099 Mainz, Germany
[21] Department of Physics and Chemistry, University of L'Aquila, 67100 L'Aquila, Italy
[22] Institute for Astroparticle Physics, Karlsruhe Institute of Technology, 76021 Karlsruhe, Germany
[23] Department of Physics and Astronomy, Purdue University, West Lafayette, IN 47907, USA
[24] Department of Physics "Ettore Pancini", University of Napoli and INFN-Napoli, 80126 Napoli, Italy
[25] Department of Physics and Astronomy, Rice University, Houston, TX 77005, USA
[26] Department of Physics, University of California San Diego, La Jolla, CA 92093, USA

^{27}Kobayashi-Maskawa Institute for the Origin of Particles and the Universe, and Institute for Space-Earth Environmental Research, Nagoya University, Furo-cho, Chikusa-ku, Nagoya, Aichi 464-8602, Japan

^{28}Department of Physics, School of Science, Westlake University, Hangzhou 310030, P.R. China

^{29}Department of Physics, Kobe University, Kobe, Hyogo 657-8501, Japan

^{30}INFN-Ferrara and Dip. di Fisica e Scienze della Terra, Università di Ferrara, 44122 Ferrara, Italy

^{31}School of Science and Engineering, The Chinese University of Hong Kong, Shenzhen, Guangdong, 518172, P.R. China

The XENONnT experiment has achieved an unprecedented reduction of the ^{222}Rn activity concentration within its liquid xenon dual-phase time projection chamber to a level of $(0.90 \pm 0.01\,\mathrm{stat.} \pm 0.07\,\mathrm{sys.})\,\mathrm{\mu Bq\,kg^{-1}}$, equivalent to about 1200 ^{222}Rn atoms per cubic meter of liquid xenon. This represents a 15-fold improvement over the ^{222}Rn levels encountered during XENON1T's main science runs and is a factor five lower compared to other currently operational multi-tonne liquid xenon detectors engaged in dark matter searches. This breakthrough enables the pursuit of various rare event searches that lie beyond the confines of the standard model of particle physics, with world-leading sensitivity. The ultra-low ^{222}Rn levels have diminished the radon-induced background rate in the detector to a point where it is for the first time lower than the solar neutrino-induced background, which is poised to become the primary irreducible background in liquid xenon-based detectors.

Keywords: Direct dark matter detection, Solar neutrino detection, Liquid xenon detectors, Low-background detectors, Radon suppression

* Also at INFN-Roma Tre, 00146 Roma, Italy

† florian.joerg@physik.uzh.ch

‡ Now at Department of Physics & Astronomy, Bucknell University, Lewisburg, PA, USA

§ Also at Coimbra Polytechnic - ISEC, 3030-199 Coimbra, Portugal

¶ michael.murra@columbia.edu

** weinheimer@uni-muenster.de

†† xenon@lngs.infn.it

I. MAIN

Deep within underground laboratories, massive detectors with ultra-low energy thresholds stand sentinel in the search for dark matter [1–7], the enigmatically abundant substance constituting nearly 85 % of the universe's mass. Although its composition remains unknown, various candidate particles are under investigation [8]. Among these are weakly interacting massive particles (WIMPs), hypothesized to possess masses ranging from hydrogen to a handful of lead atoms [9]. While interactions with ordinary matter are expected to be rare, theoretical models predict that WIMPs could occasionally scatter elastically off atomic nuclei, imparting a characteristic recoil energy on the order of a few keV.
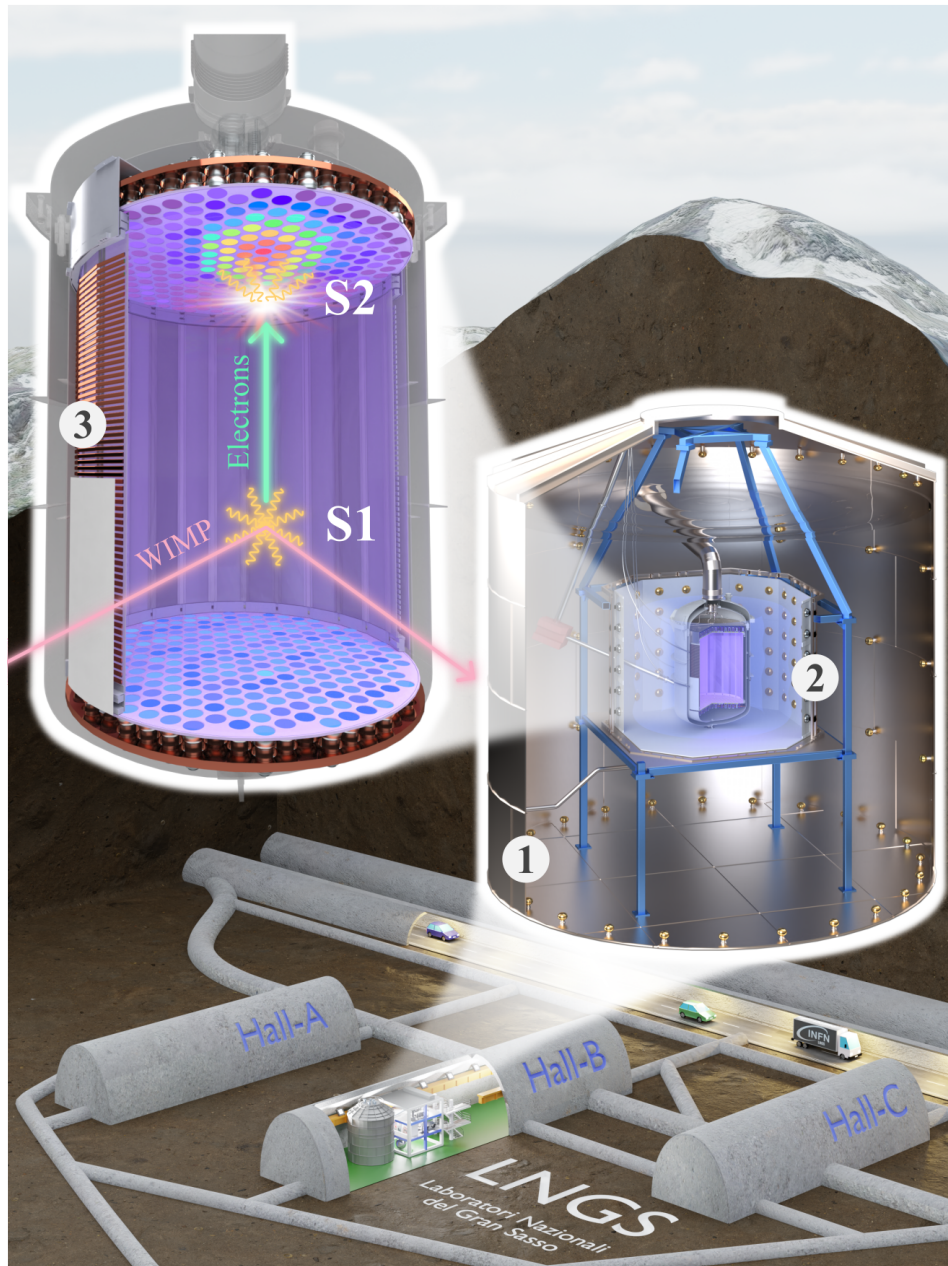
FIG. 1. Schematic overview of the XENONnT experiment: The experiment is located 1400 m underground at the Laboratori Nazionali del Gran Sasso (LNGS), Italy. This depth significantly reduces cosmic muon and neutron backgrounds due to rock overburden. The experimental setup consists of a service building housing the xenon handling and data acquisition systems, and a water tank containing three nested detectors: (1) The muon veto, (2) the neutron veto, and (3) the Time Projection Chamber (TPC). The TPC is the central detector, measuring low-energy particle interactions in the LXe volume. Its key features include deposited energy measurement, particle identification, and 3D position reconstruction.

Detecting these faint signals directly requires both exceptional sensitivity and the ability to differentiate them from background events like radioactive decays or cosmic muons.

Dual-phase xenon time projection chambers (TPCs), pioneered by the XENON collaboration [1, 10–12] and others [4, 13–15], have proven to be highly effective for this purpose. Upon WIMP interaction with the liquid xenon (LXe) target, a prompt scintillation light (S1) is emitted and detected by two photosensor arrays at the top and bottom of the TPC (Figure 1 inset). Additionally, free electrons from the interaction drift upwards in an electric field to the liquid-gas interface. Here, a 20-fold stronger extraction field pulls them into the gaseous xenon (GXe) and accelerates them, inducing electroluminescence: The electrons excite the xenon atoms, producing a delayed and even brighter flash of light (S2), also detected by the photosensors. The location in the horizontal plane is obtained from the S2 signal distribution recorded by the upper photosensor array, while the time difference between S1 and S2, inversely proportional to the known electron drift velocity, provides the vertical coordinate. Thanks to the substantial shielding offered by LXe's high density (about three times that of water), radioactivity from detector materials can be largely suppressed by restricting analysis to the central region of the target (fiducialization). By combining the S1 and S2 signals, the deposited energy of an interaction can be precisely reconstructed, allowing for an energy threshold of $\mathcal{O}(1)$ keV. Moreover, the S2/S1 ratio helps discriminate WIMP-nucleus scattering (nuclear recoil, NR) from background events like beta/gamma scattering on electrons (electronic recoil, ER). This combination of high efficiency, low energy threshold, and excellent background rejection makes the xenon TPC technology a powerful tool for WIMP and other rare event searches.

Its potential, coupled with the captivating nature of the scientific question, has spurred continued advancements. Nearly two decades after the ZEPLIN-II [13] and XENON10 [10] experiments with approximately 10 kg xenon targets, three currently operational experiments — PandaX-4T [6], XENONnT [1], and LZ [4] — have emerged. Leveraging active LXe masses ranging from 4 to 7 tonnes, these experiments search for WIMPs and other rare phenomena within underground laboratories across China, Italy, and the USA. Additionally, a similar argon-based experiment, DarkSide-20k [16], is under construction in Italy.

Beyond WIMPs, the xenon TPC technology tackles another equally crucial and timely science question: the search for neutrinoless double beta decay [17]. This elusive process holds the key to unlocking the universe's matter-antimatter asymmetry and the remarkably small mass of neutrinos. Like WIMP searches, it demands exceptional sensitivity and background reduction, but at higher signal energies of a few MeV. Building upon the successful EXO-200 experiment [18], the nEXO experiment [19] is planned for the Canadian underground laboratory, SNOLAB. This next-generation detector will contain 5 tonnes of LXe enriched in the isotope ^{136}Xe, a promising candidate for neutrinoless double beta decay, offering a massive target for the rare decay. As with WIMPs, the decisive factor here is the ultra-low background rate alongside the large isotope mass.

These experiments aim to detect a handful of rare events above the detector background over their operational lifetime. Consequently, minimizing background is crucial and involves multiple steps. Experiments are positioned in underground laboratories to reduce exposure to cosmic muons and are further shielded with active veto systems, typically based on large water or liquid scintillator volumes, to identify muons and neutrons. Stringent material selection ensures minimal radioactivity within the detector itself. After fiducialization and advanced event discrimination techniques, only background sources remain that cannot be shielded or are dissolved in the LXe itself. The first category includes solar and atmospheric neutrinos. The second category includes radioactive isotopes such as ^{3}H, ^{37}Ar, ^{39}Ar, ^{85}Kr, ^{220}Rn and ^{222}Rn dissolved in LXe. Entry points include xenon extraction from air separation, emanation from detector materials, or air leaks. Noble gas impurities cannot be easily mitigated by conventional noble gas purifiers, e.g. high-temperature getters. Additionally, long-lived isotopes like ^{124}Xe and ^{136}Xe with half-lives longer than 10^{20} years are present within the xenon. The decay of ^{124}Xe via double electron capture has been observed for the first time with the XENON1T experiment [20, 21], XENONnT's predecessor, and offers valuable calibration opportunities for future generations of detectors. The two-neutrino double beta decay of ^{136}Xe remains a non-negligible background source for dark matter searches [3].

Previous work by the XENON Collaboration demonstrated effective removal of lighter noble gases like argon and krypton from LXe using cryogenic distillation, achieving negligible concentrations [22]. However, a one-time removal is not sufficient for radon isotopes, that continuously emanate from detector materials due to the decay chains of primordial uranium and thorium present in virtually all materials.

The longest-lived radon isotope ^{222}Rn with its half-life of 3.8 d [23] poses the most significant background challenge for dark matter and neutrinoless double beta decay searches in xenon detectors. Their decay progeny present particular difficulties. For example, the beta decay of the daughter isotope ^{214}Pb deposits energy as an ER in the TPC. This background cannot be sufficiently eliminated through an S2/S1 ratio cut, which currently achieves 99.3 % efficiency in XENONnT at a 50 % NR signal acceptance [2]. Notably, the remaining ER signals cannot be differentiated from potential WIMP interaction signals. Similarly, for the neutrinoless double beta decay search in ^{136}Xe, the major background arises from the gamma line emitted by another radon progeny, ^{214}Bi, whose energy falls close to the expected Q-value of the double beta decay.

In XENON1T's main science run, the ^{222}Rn activity concentration stood at $(13.3 \pm 0.5)\,\mu$Bq kg^{-1}. An R&D run achieved a lower value of $(4.5 \pm 0.1)\,\mu$Bq kg^{-1} through two key innovations: first, the existing GXe purification pumps were exchanged with a novel, nearly radon-free, magnetically-coupled piston pump [24], and second, radon was actively removed by operating the krypton distillation system in inverse mode [25].

The XENONnT experiment demands a ^{222}Rn activity concentration of $1\,\mu$Bq kg^{-1}, translating to just one ^{222}Rn atom per 16 moles xenon. The XENONnT strategy is multifaceted: the first line of defense is material selection to minimize radon emanation from the outset, followed by an inherent surface-to-volume advantage of the larger detector volume compared to XENON1T, and finally, active removal to eliminate any remaining radon and to reach the desired level.

Beyond WIMP searches, this exceptionally low ^{222}Rn level opens doors to a diverse physics program utilizing ER events [3]. World-leading sensitivity is attainable for various searches, including solar axions, neutrino magnetic moment, bosonic dark matter (dark photons, ALPs), low-mass WIMPs via the Migdal effect, and low energy ER peak searches. Furthermore, the solar neutrino-induced rate in the detector would match the radon-induced one. Further reducing the ^{222}Rn activity concentration remains crucial for solar neutrino and double beta decay searches [26] but would provide less improvement for WIMP and low energy ER searches.

This paper focuses on demonstrating the potential of the newly developed cryogenic distillation-based Radon Removal System to continuously keep XENONnT's radon concentration at a sub-μBq kg^{-1} level. The removal strategy and system are detailed in section II. The removal efficiency is directly measurable and quantifiable through in-situ alpha decay measurements using the TPC, as presented in section III. This allows for a direct comparison of the various removal modes to the one without removal. The impact on future detectors is discussed in section IV.

II. RADON REMOVAL IN XENONNT

The XENONnT experiment [1] is more than just a LXe TPC housed in a cryostat, surrounded by veto detectors. It is equipped with a variety of xenon handling systems, as shown in Figure 2. A cryogenic system (CRY) is required to maintain thermodynamic equilibrium of the xenon within the detector at a temperature around $-100\,°$C. This CRY system comprises two pulse tube refrigerators and an emergency liquid nitrogen (LN$_2$) cooling tower connected to the inner cryostat via a cryopipe to balance evaporated xenon resulting from external heat input by condensation. Cable feedthrough vessels connected to the cryopipe contain high voltage and signal cables for the photomultiplier tubes (PMTs) inside the detector.

Furthermore, two purification systems are used to continuously clean the xenon. LXe from the detector is extracted and evaporated via a series of heat exchangers before being purified from electronegative impurities using a gas purification system (GXe-PUR) comprising a radon-free GXe pump and getter-based purifier. In parallel, a novel LXe purification loop (LXe-PUR) circulates LXe through purifiers using a cryogenic liquid pump, also to remove electronegative impurities. The detector's LXe volume containing around 8500 kg of xenon can be exchanged once per day by the LXe-PUR system. While most of the xenon through the LXe-PUR system is returned to the cryopipe and subsequently to the detector, a fraction is directed to the Radon Removal System (RRS) to reduce the ^{222}Rn activity concentration in the detector.

All internal surfaces in contact with GXe or LXe are potential sources of radon, which continuously emanates into the xenon target material. Dedicated radon emanation measurements [25, 27] reveal the location and magnitude of different radon sources in the XENONnT system. The sources are classified into two main types, depending on their position in the XENONnT system relative to the RRS. Type 1 sources emanate and are flushed directly into the detector before reaching the RRS. They are further subdivided into type 1a sources, which go directly into the cryostat's LXe, and type 1b sources, which are within the cryostat's and CRY system's GXe phase. A radon source upstream of the RRS in the xenon handling system is referred to as type 2. Consequently, type 2 radon enters the RRS before reaching the LXe inside the detector, and can therefore be efficiently removed. The classification of the different subsystems in XENONnT is highlighted in Figure 2. Subcomponents of a subsystem can contribute to different source types (Methods).

The center part of XENONnT's RRS is a cryogenic distillation column [28], exploiting the difference in vapor pressure between xenon and radon. Radon, the less volatile component, accumulates in the LXe at the bottom of the column, where it is trapped until decay. To significantly reduce radon and mitigate its decay-induced background signals in the LXe TPC, the RRS process flow must be sufficiently large to purify the TPC's LXe mass on a timescale comparable to or shorter than the radon decay constant (5.5 days). A LXe extraction flow of about $71\,$kg h^{-1} through the RRS would correspond to a 2-fold radon reduction for type 1 radon sources given the 8500 kg xenon in the cryostat [28]. The radon-depleted xenon can be extracted in gaseous form from the top condenser of the RRS, which is operated with liquid nitrogen providing about 1 kW of cooling power. A LXe reflux is created at the top of the column by partially re-condensing the evaporated xenon coming from the reboiler at the bottom. This enhances the
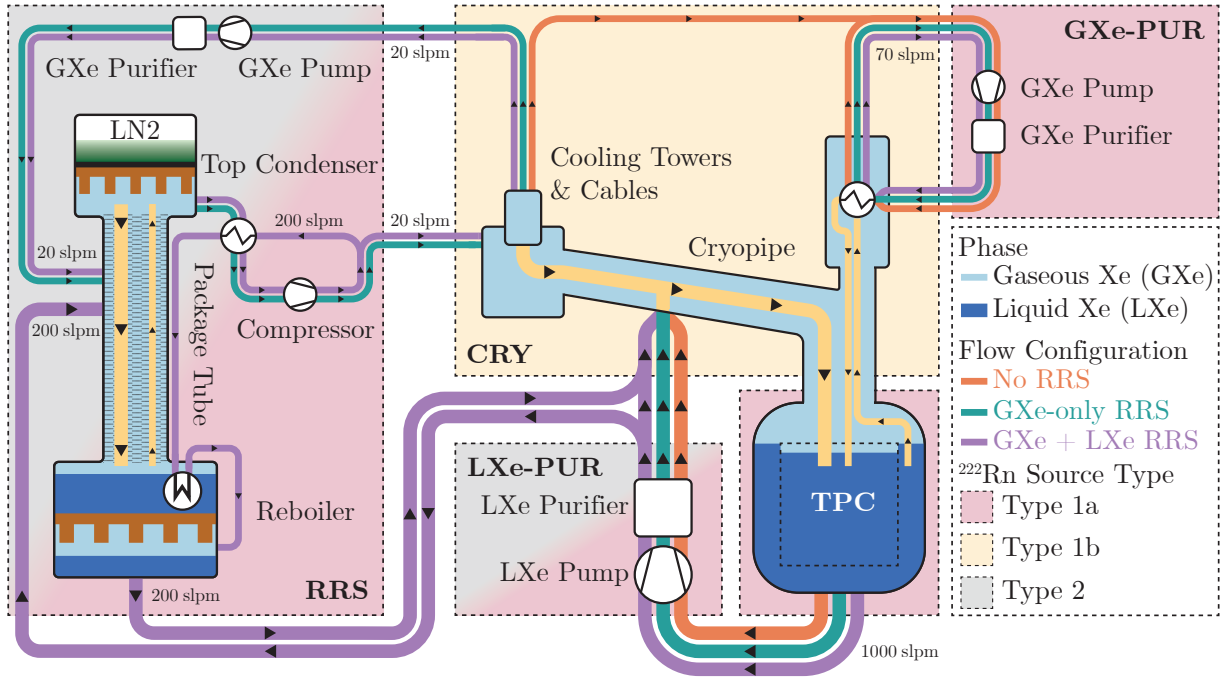
FIG. 2. Online Radon Removal System and operational modes. The figure depicts the xenon handling systems and their interplay for continuous purification of the xenon inside the Time Projection Chamber (TPC). Xenon circulation (thin/thick lines for gaseous xenon (GXe)/liquid xenon (LXe)) is maintained via dedicated pumps (GXe/LXe) and purification systems (GXe-PUR/LXe-PUR) to remove electronegative impurities. Internal xenon flows are highlighted in yellow. A cryogenic distillation column-based Radon Removal System (RRS) targets radon emanating from various subsystems categorized by source types 1a (red), 1b (beige), and 2 (gray). Three operational modes are highlighted: In the *No RRS* mode (orange), the RRS is bypassed, and all radon emanated enters the TPC. In the *GXe-only RRS* mode (teal), radon-rich GXe is extracted from the cryogenic system (CRY) and directed to the RRS for purification. The radon-depleted GXe is then returned to the CRY system. In the *GXe+LXe RRS* mode (violet), a portion of LXe from the LXe-PUR is diverted to the RRS. The resulting radon-depleted GXe is liquefied and fed back into the LXe-PUR system.

column's separation efficiency and reduces the probability of radon atoms escaping the column's top and spoiling the radon-depleted xenon exhaust. The extracted radon-depleted xenon flow must be liquefied again at the RRS output before it returns to the detector requiring an additional 2 kW of cooling power. To address this significant energy demand, an energy-efficient solution was crucial. Therefore, a cryogenic heat pump concept was developed to condense the radon-depleted xenon, achieving a 3-fold reduction in externally supplied cooling power (Methods).

The radon removal strategy has two modes: In the LXe-mode, a LXe flow is continuously extracted from the detector, purified with the RRS, and fed back as radon-depleted LXe. This mode is projected to achieve a 2-fold reduction in radon concentration. In the GXe-mode, xenon is extracted from the GXe phase before entering the detector's LXe phase, effectively converting type 1b sources into type 2 sources that go directly to the RRS [25]. This mode potentially achieves another factor-of-two reduction in ^{222}Rn activity concentration depending on the extraction efficiency. Three operational modes that were performed in XENONnT are visualized in Figure 2:

a) **No RRS:** The RRS system is not in operation (orange).

b) **GXe-only RRS:** Only GXe extraction is performed (teal).

c) **GXe+LXe RRS:** A combination of GXe and LXe extraction is performed (violet).

III.   RADON ALPHA DECAYS IN XENONNT

Radon is a primordial decay product, arising from both the uranium and thorium decay chains. The isotopes ^{219}Rn and ^{222}Rn are produced in the uranium chains of ^{235}U and ^{238}U, respectively, while ^{220}Rn originates from the thorium chain ^{232}Th. Due to its short half-life of less than 4 s [23], ^{219}Rn decays before it reaches the central xenon volume and does not pose a background source for the dark matter search. The decay chains starting from the other two isotopes ^{220}Rn and ^{222}Rn are highlighted in Figure 3 (top). The decay chain of ^{222}Rn includes several alpha and beta emitters. While alpha particles have distinct MeV energies, beta particles possess continuous spectra up to their endpoints of a few hundreds of keV, which can be misinterpreted as low-energy WIMP signals. Among these emitters, ^{214}Pb stands out due to its 12.7 % branching ratio for beta decay to the ground-state without accompanying gamma emission [29]. This decay mode poses a significant background source since all other beta decays of the uranium and thorium decay chains are either identifiable by time-coincident alpha or gamma decays, or involve decays with
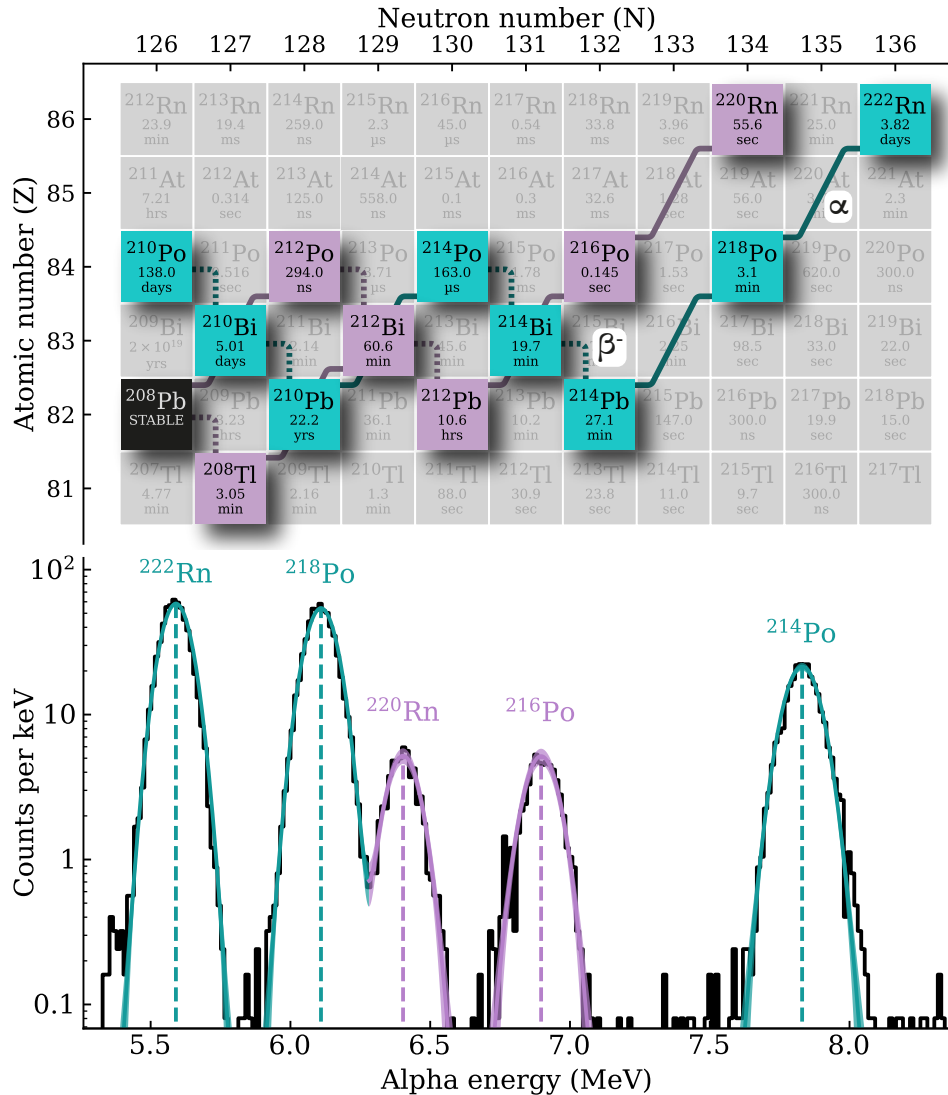

FIG. 3. **Top:** ^{222}Rn (teal) and ^{220}Rn (violet) decay chains as part of the primordial uranium and thorium chains. Alpha (α) decays are indicated by solid lines, while beta (β⁻) decays are indicated by dashed lines. Note that while the decay chains appear to intersect, each isotope belongs exclusively to either the ^{222}Rn or the ^{220}Rn decay chain. All values are taken from Ref. [23]. **Bottom:** Reconstructed energy spectrum of alpha decays in the XENONnT detector. The relative energy resolution is better than 1%, allowing to distinguish the alpha decays of different isotopes within the ^{222}Rn and ^{220}Rn decay chains. The fit of the data is done with Gaussian functions. Ionized progenies from the decay chains partly plate out on the cathode and detector walls under the influence of the electric field and due to LXe convection. This results in reduced concentrations in the LXe bulk for isotopes further down the decay chain such as ^{214}Po.

longer half-lives, like the one of ^{210}Pb. While the XENONnT detector is optimized for the detection of low-energy interactions in the keV region, its sensitivity extends well into the MeV range, enabling in-situ measurements of the alpha decays (see Figure 3, bottom).

The full decay energy Q_α of alpha particles is deposited in the LXe. However, due to their high stopping power, alpha particles produce short tracks ($\leq 100\,\mu$m) with a high density of electron-ion pairs [30]. As a consequence, most of them recombine, resulting in a reduced S2 charge signal and an enhanced S1 scintillation signal. Since the number of detected scintillation photons is large ($\sim 50\,000$ photons), alpha particles can be detected using only the S1 signal (Methods). The Figure 3 shows the energy spectrum of alpha particles detected in the LXe. As expected, the three alpha emitting isotopes ^{222}Rn, ^{218}Po, and ^{214}Po from the uranium chain are observed. Additionally, the spectrum shows a subdominant contribution from ^{220}Rn and ^{216}Po, as well as from ^{212}Po (not shown in the figure), which belong to the thorium decay chain.

To determine the time-dependent evolution of the ^{222}Rn activity, a $\pm 3\,\sigma$ region around the ^{222}Rn peak is selected and events falling within this region are counted as a function of time. Generally, it is more informative to report the activity concentration rather than the activity. To achieve this, the measured activity in terms of µBq is divided by the sensitive analysis volume (Methods) to normalize it to the fiducial LXe mass.
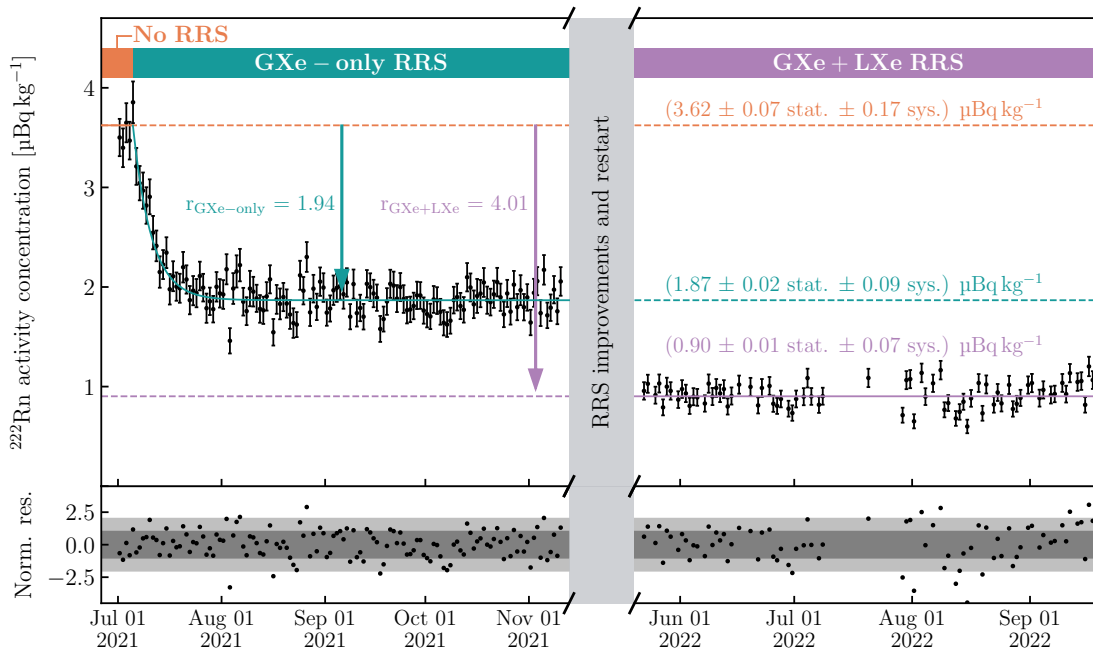

FIG. 4. ^{222}Rn activity concentration in XENONnT. This figure shows the ^{222}Rn activity concentration (black) in XENONnT as a function of time for the three operational modes: *No RRS* (orange), *GXe-only RRS* (teal), and *GXe+LXe RRS* (violet). A radon removal model is included as a solid line (Methods). Normalized residuals are displayed in the bottom panel. The gray shaded area denotes a period where improvements were made to the Radon Removal System (RRS) and stable data acquisition was not possible. Radon reduction factors within the Time Projection Chamber (TPC) are estimated as $r_{\text{GXe-only}} = (1.94 \pm 0.04)$ and $r_{\text{LXe+GXe}} = (4.01 \pm 0.28)$ for *GXe-only RRS* and *GXe+LXe RRS* modes, respectively. The minimum ^{222}Rn activity concentration of $(0.90 \pm 0.01\,\text{stat.} \pm 0.07\,\text{sys.})\,\mu\text{Bq}\,\text{kg}^{-1}$ is the lowest ever achieved in an operational LXe TPC. It depends on the RRS process flow and detector conditions. Data points include statistical uncertainties (Methods). The statistical uncertainty in achieved ^{222}Rn activity concentrations within each mode is calculated from the model fit via bootstrapping, and the systematic uncertainties are derived from the in-situ alpha decay analysis (Methods).

The Figure 4 depicts the ^{222}Rn activity concentration over time, encompassing the three periods corresponding to the *No RRS* (orange), *GXe-only RRS* (teal), and *GXe+LXe RRS* (violet) modes. Without the implementation of any active RRS, the activity concentration is around $(3.62 \pm 0.07\,\text{stat.} \pm 0.17\,\text{sys.})\,\mu\text{Bq}\,\text{kg}^{-1}$, which is similar to the estimated value of $4.2^{+0.5}_{-0.7}\,\mu\text{Bq}\,\text{kg}^{-1}$, inferred from emanation measurements carried out at room temperature [25]. During the initial science run of XENONnT [2, 3], the *GXe-only RRS* mode yielded an activity concentration of $(1.87 \pm 0.02\,\text{stat.} \pm 0.09\,\text{sys.})\,\mu\text{Bq}\,\text{kg}^{-1}$. For the second science run, the full extent of the radon removal capabilities was employed, resulting in a remarkable reduction of the activity concentration to $(0.90 \pm 0.01\,\text{stat.} \pm 0.07\,\text{sys.})\,\mu\text{Bq}\,\text{kg}^{-1}$, better than the desired design value of $1\,\mu\text{Bq}\,\text{kg}^{-1}$. This represents a substantial decrease of a factor of (4.01 ± 0.28) compared to the initial concentration observed under the *No RRS* mode.

IV.   IMPACT FOR FUTURE DETECTORS

LXe-based dark matter experiments have witnessed a significant increase in target mass from approximately $10\,\mathrm{kg}$ two decades ago to the current range of several tonnes. Next-generation detectors are under design to reach up to 60 tonnes or more target mass. The Figure 5 presents the evolution of $^{222}\mathrm{Rn}$ activity concentration across various experiments, including those searching for neutrinoless double beta decay, as a function of target mass. As detector target mass steadily increased over time, the $^{222}\mathrm{Rn}$ activity concentration exhibited a decrease following the expected improvement due to the surface-to-volume ratio enhancement in larger detectors. Nevertheless, a substantial improvement was only achieved when active removal was implemented, as demonstrated in XENONnT.

In comparison to the $^{222}\mathrm{Rn}$ activity concentration in XENON1T of $(13.3 \pm 0.5)\,\mathrm{\mu Bq\,kg^{-1}}$ during its main science runs, a 15-fold reduction was accomplished in XENONnT. In comparison to other tonne-scale detectors currently in operation, a 5-fold reduction was achieved. Note that the ER background due to the $^{214}\mathrm{Pb}$ beta decay can be further mitigated through the implementation of a radon tagging analysis [39, 40].
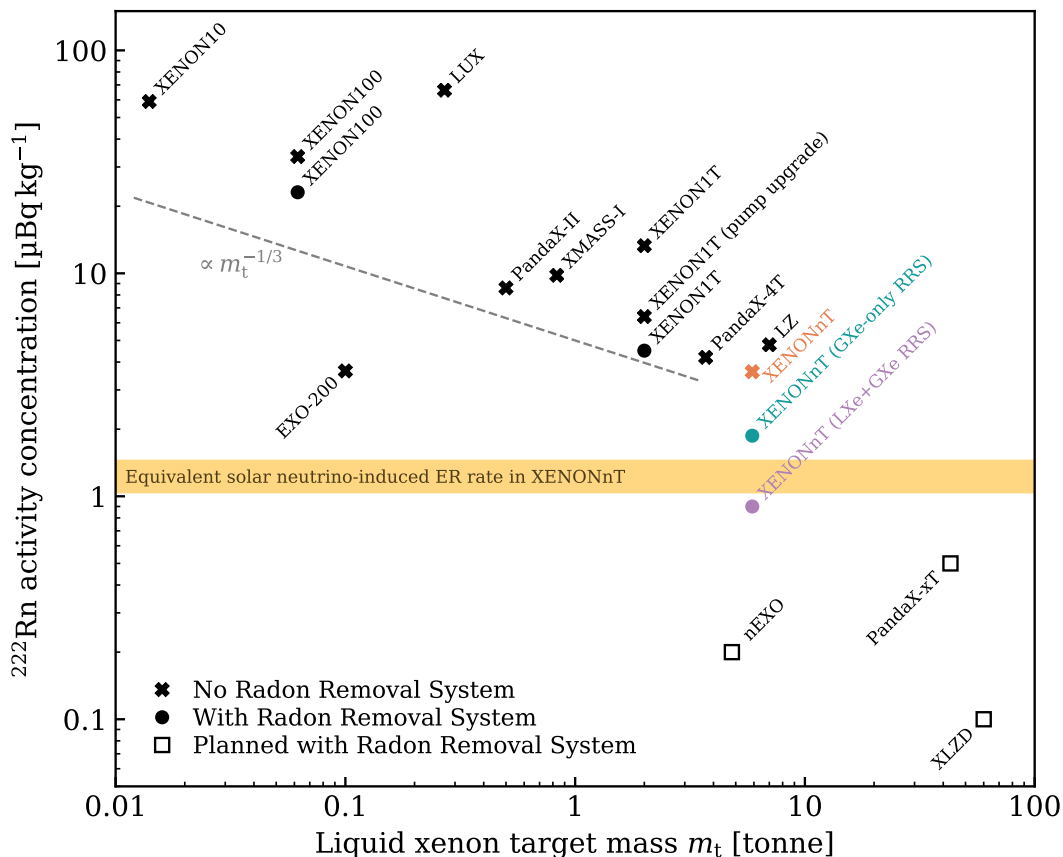

FIG. 5. $^{222}\mathrm{Rn}$ activity concentration in LXe-based experiments as a function of their LXe target mass. Crosses indicate experiments without a dedicated Radon Removal System (RRS), while full circles represent those with active RRS. Open squares depict projected/required values for future experiments. The gray dashed line visualizes a surface-to-volume improvement trend scaling with $m_{\mathrm{t}}^{-1/3}$: As detector size increases, the target volume scales cubically, while the radon-emitting surface scales quadratically, leading to a lower $^{222}\mathrm{Rn}$ activity concentration within the target volume. Experiments with active RRS, like XENONnT (teal, violet) demonstrably deviate from this trend, achieving significantly lower levels. EXO-200, searching for neutrinoless double beta decay, is an exception, achieving a significantly lower $^{222}\mathrm{Rn}$ level compared to similar-sized experiments probably due to its liquid-only phase detector design, which minimized type 1 $^{222}\mathrm{Rn}$ sources directly impacting the active target mass. The yellow band represents the equivalent solar neutrino-induced ER rate in XENONnT (in units of $\mathrm{\mu Bq\,kg^{-1}}$), considering uncertainties in current solar neutrino-xenon interaction models (Methods). Data sources include XENON10 [10], XENON100 [31], EXO-200 [32], LUX [33], PandaX-II [34], XMASS-I [35], XENON1T [25], PandaX-4T [6], XENONnT (this work), LZ [36], nEXO [19], PandaX-xT [37], and XLZD [38].

The reported reduction of the ^{222}Rn activity concentration by XENONnT to $(0.90 \pm 0.01 \,\text{stat.} \pm 0.07 \,\text{sys.}) \,\mu\text{Bq}\,\text{kg}^{-1}$ is a critical milestone in low-energy rare event experiments: The ^{222}Rn level achieved is so low that the background induced by the unshieldable solar neutrinos is for the first time comparable to the ^{222}Rn-induced background. Solar neutrinos, generated in the Sun's core via fusion reactions, produce a particle flux of approximately $7 \times 10^{10} \,\text{s}^{-1} \,\text{cm}^{-2}$ at Earth. The majority originate from the proton-proton chain and exhibit characteristic energy spectra extending to several MeV [41]. While predominantly traversing LXe detectors without interaction, a subset induce NRs through coherent elastic neutrino-nucleus scattering (CEνNS), mimicking WIMP signals. Recent CEνNS measurements of solar ^{8}B neutrinos by XENONnT and PandaX-4T [42, 43] underscore the importance of this background. Additionally, solar neutrinos can scatter off electrons, creating low-energy ERs. Solar neutrino ER interactions, previously obscured by the dominant ^{214}Pb background, could now be directly observed in LXe detectors. This fact is illustrated by the yellow band in Figure 5, which denotes an equivalent solar neutrino-induced rate in XENONnT in units of $\mu\text{Bq}\,\text{kg}^{-1}$, encompassing the uncertainties associated with current solar neutrino interaction models with xenon (Methods).

XENONnT's groundbreaking achievement of an ultra-low radon level below $1 \,\mu\text{Bq}\,\text{kg}^{-1}$ opens exciting avenues for exploration beyond the Standard Model such as the search for elusive particles like solar axions, axion-like particles, dark photons, and an enhanced neutrino magnetic moment [3]. Furthermore, the successful development and implementation of XENONnT's high-flow Radon Removal System paves the way for future detectors like PandaX-xT [37] or XLZD [38] with 40 to 60 tonnes of LXe. Such an experiment holds immense potential as the ultimate observatory for low-energy astroparticle physics. Its capabilities will range from precise solar neutrino studies through neutrino-electron and coherent elastic neutrino nucleus scattering, to searches for extremely rare processes like double weak decays of the xenon isotopes ^{124}Xe and ^{136}Xe, particularly its neutrinoless double beta decay. Additionally, it could probe a wide range of dark matter candidates, including WIMPs, down to the elusive neutrino fog — the theoretical limit where the dark matter signal becomes indistinguishable from the irreducible background of solar and atmospheric neutrinos [44].

V. METHODS

A. Radon Removal System: Working Principle

The XENONnT Radon Removal System, shown in Figure 6, leverages a cryogenic distillation column with a design flow rate of $71 \, kg \, h^{-1}$ (200 slpm) to significantly reduce the impurity radon in the LXe target in the detector. It is designed to operate mainly with LXe input and output. Radon reduction is achieved by effectively trapping radon in a dedicated LXe reservoir at the bottom of the column. The relatively short half-life of radon (3.8 d) ensures its decay within the reservoir, eliminating the need for extraction of the impurity-enriched xenon, unlike in conventional distillation systems for krypton or argon removal [22]. This feature makes the radon removal process inherently xenon-loss-free allowing for a continuous operation. The distillation tower comprises three key components: a top condenser, a central package tube, and a bottom reboiler. The reboiler houses the LXe reservoir (capacity: up to 130 kg) where radon accumulates due to its 10-fold lower vapor pressure compared to xenon at $-100 \, °C$ [45]. The reboiler also employs electrical heaters to vaporize a portion of the LXe, creating an upward gas stream (flow rate: $106 \, kg \, h^{-1}$ (300 slpm)) through the package tube. This tube contains a structured packing material with a large surface area for efficient liquid-gas exchange across its entire height (190 cm), effectively acting as a series of interconnected theoretical distillation stages [28].

Radon-rich LXe and GXe from the detector enter the mid-section of the tube. The liquid flows downward to the reboiler, while the gas ascends towards the top condenser. Here, a portion of the upward gas stream from the reboiler and the feed condenses and flows back to the package tube at a rate of $35 \, kg \, h^{-1}$ (100 slpm), maintaining a LXe reflux ratio of 0.5 relative to the $71 \, kg \, h^{-1}$ (200 slpm) radon-depleted xenon extraction flow. This rectification process prevents radon escape from the top.

The system is designed to achieve a 1000-fold radon enrichment between the feed and the reboiler, and a 100-fold reduction between the feed and the top condenser. With the chosen design parameters, including process flow, reflux ratio, and inlet and outlet radon concentrations, the McCabe-Thiele method allowed calculation of the required number of theoretical distillation stages and consequently the total height of the packed column [28]. Further, the necessary cooling and heating powers were derived to facilitate xenon phase changes throughout the system.

The top condenser requires approximately 1 kW of cooling power to maintain the desired reflux ratio of 0.5 and is achieved with a custom-made bath-type heat exchanger operated with liquid nitrogen [46]. The extracted radon-depleted GXe flow of $71 \, kg \, h^{-1}$ (200 slpm) from the top condenser must be reliquefied for reinjection into the LXe purification circuit. This additional liquefaction step necessitates another 2 kW of cooling power, bringing the total
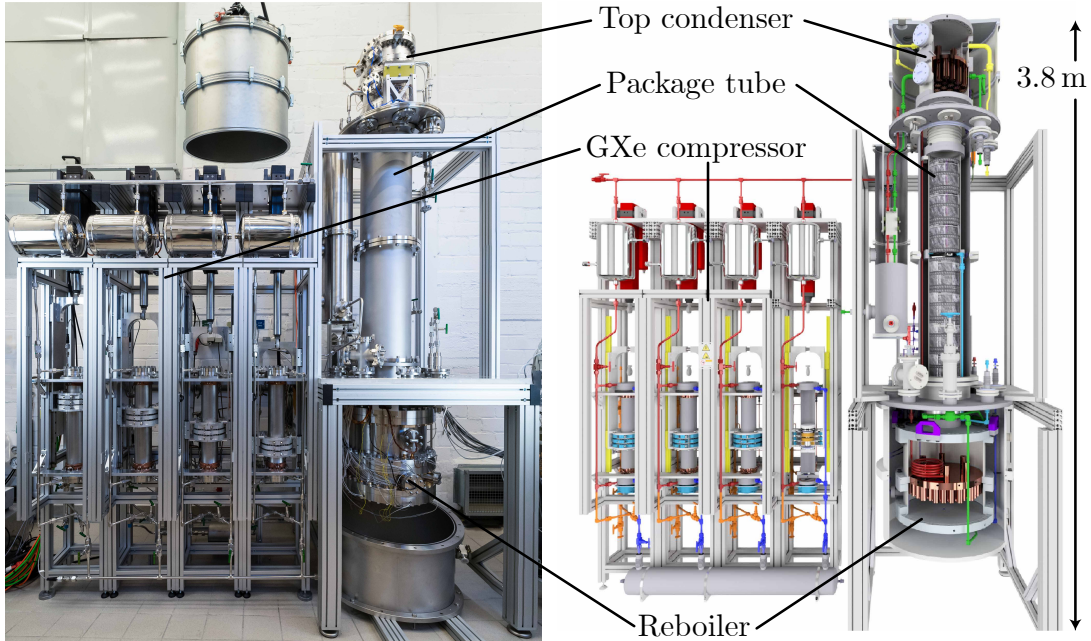

FIG. 6. Radon removal system constructed and set up at University of Münster before shipping to LNGS (left) and related CAD drawing (right). The four key components top condenser, package tube, reboiler and GXe compressor for the heat pump, composed of a four-cylinder magnetically-coupled piston pump, are visible. Based on Ref. [28].

cooling requirement to 3 kW. The reboiler, on the other hand, requires 3 kW of heating power to generate the upward evaporation flow of $106 \, \mathrm{kg \, h^{-1}}$ (300 slpm), vital for a stable distillation process within the package tube.

The substantial cooling power required for the xenon liquefaction at the outlet necessitates an energy-efficient solution. This is achieved through the heat pump principle: gaseous radon-depleted xenon from the top is first compressed with a GXe compressor and is then liquefied in a novel bath-type GXe-LXe heat exchanger (HE) integrated into the reboiler. This HE features two compartments: a top vessel containing LXe and a bottom vessel holding radon-depleted GXe. By thermally connecting these compartments, the GXe condenses in the bottom while LXe evaporates in the top, eliminating the need for the additional 2 kW of electric heating. This heat exchange process relies on a temperature difference and thus a pressure difference between the compartments. The GXe pressure must be higher than the LXe pressure, allowing the GXe to condense at a higher temperature and establish the necessary temperature gradient that drives heat transfer. To achieve this pressure differential, a four-cylinder magnetically coupled piston pump is employed as a compressor [47]. Additional GXe/GXe HEs further optimize the system efficiency by pre-cooling and pre-warming the GXe flow between the tower and the compressor. XENONnT's demanding radiopurity requirements, ensuring the RRS itself does not contribute significantly to the radon in the detector, necessitated rigorous material screening and custom fabrication of most system components. This included the two HEs at the top and bottom, the package tube, as well as the compressors.

The RRS system underwent extensive commissioning in an internal bypass configuration, where the RRS liquid outlet was internally connected with its liquid inlet. Under thermodynamically stable conditions, the system operated at a flow rate of $(91 \pm 2) \, \mathrm{kg \, h^{-1}}$ $((258 \pm 6) \, \mathrm{slpm})$. This represents a 30% increase above the design flow rate for the XENONnT operation, validating the system's capacity for extended performance and potential flexibility [28].

B.   In-situ ^{222}Rn Activity Concentration Measurement

For this analysis, only the scintillation signal S1 was utilized (S1-only method), allowing continuous ^{222}Rn activity concentration monitoring even when the charge signal S2 was unavailable, e.g. when no extraction field was present. Given that alpha particles produce highly localized, high-energy interactions, their energy can be reconstructed solely from the S1 signal. However, event position reconstruction within the TPC based solely on S1 exhibits larger systematic uncertainties compared to the standard S1+S2 method [48]. To address this, two independent ^{222}Rn activity concentration analyses (I and II) were conducted. Both are outlined in the following, with their main difference being the chosen method for the event position reconstruction.

The S1 light collection efficiency for alpha events varies with their location within the detector due to total internal reflection at the liquid-gas interface and reflections off the detector walls. Spatial dependence corrections were derived using either the monoenergetic alpha decays of ^{214}Po or ^{222}Rn. Their signal dependencies along the radial and depth coordinate were fit using polynomial models. Due to an increased concentration of photoabsorbing impurities in the LXe during the *GXe+LXe RRS* mode, an additional correction to the observed number of photons per alpha event (less than 5%) was applied (see [42] for further details).

The event position reconstruction differed between the two analyses: In Analysis-I, the horizontal position was determined from the center of mass of the light distribution recorded by the top and bottom PMT arrays. The depth was inferred from the fraction of light detected by the top array relative to the total detected light (see Figure 7), with a lower fraction indicating a deeper event position. Analysis-II employed a convolutional neural network (CNN) algorithm, trained on data with S2-derived event locations, to reconstruct both horizontal and vertical coordinates [49].

To mitigate the influence of alpha decays from ^{210}Po accumulating on the detector walls and electrodes, both analyses were restricted to an inner volume, containing a LXe mass of $m_{\mathrm{S1\text{-}only,I}} = (1.22 \pm 0.03) \, \mathrm{t}$ for Analysis-I and $m_{\mathrm{S1\text{-}only,II}} = (2.05 \pm 0.06) \, \mathrm{t}$ for Analysis-II. This mass was estimated using a reference dataset containing events with both S1 and S2 information. S2-derived event positions were used to define a reference volume V_{ref} encompassing the volumes selected using the S1-only information. The masses $m_{\mathrm{S1\text{-}only,i}}$ were then determined by scaling the reference volume, V_{ref}, according to the ratio of ^{222}Rn decays observed within the S1-only selected volume $N_{\mathrm{S1\text{-}only,i}}$, to those observed within the reference volume N_{ref}

$$m_{\mathrm{S1\text{-}only,i}} = V_{\mathrm{ref}} \cdot \rho_{\mathrm{LXe}} \cdot \frac{N_{\mathrm{S1\text{-}only,i}}}{N_{\mathrm{ref}}} \qquad i = \{\mathrm{I, II}\}, \tag{1}$$

where ρ_{LXe} denotes the density of liquid xenon at the operating temperature and pressure of the detector. The systematic uncertainty of $m_{\mathrm{S1\text{-}only,i}}$ contains the uncertainty in the $N_{\mathrm{S1-only,i}}/N_{\mathrm{ref}}$ ratio, as well as contributions from of S1+S2 position reconstruction precision, LXe density variations, and electric field distortions, as detailed in Ref. [48].
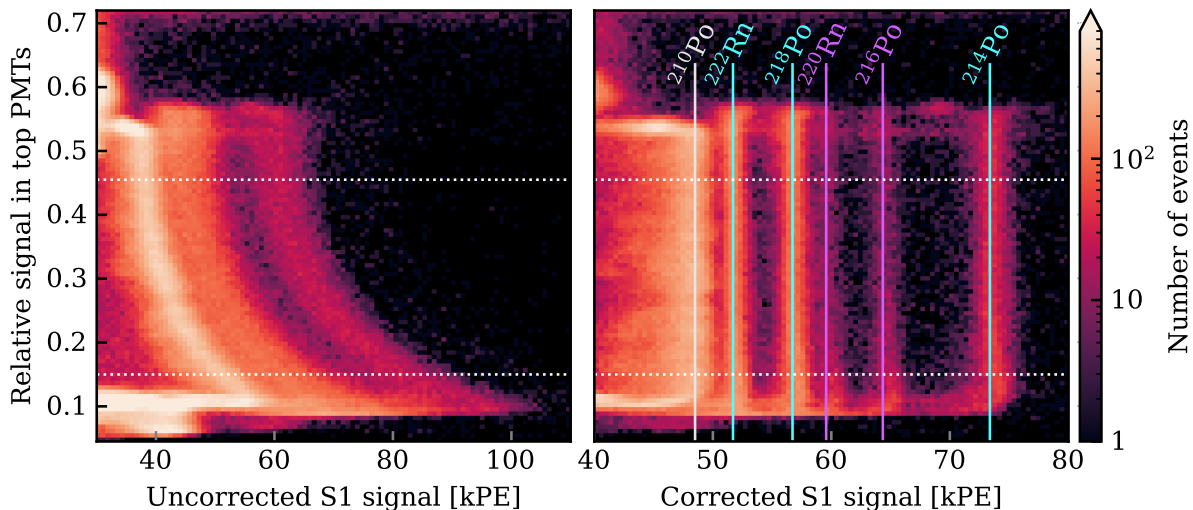
FIG. 7. Scintillation signal of alpha interactions in the XENONnT detector. **Left:** Depth dependence of the uncorrected light signal. **Right:** Same data after all geometric corrections from Analysis-I are applied (see text). The horizontal dashed lines indicate the selected subvolume used for the analysis.

The Figure 3 presents the reconstructed monoenergetic alpha peaks using the Analysis-I corrections, fitted with a sum of individual Gaussian functions. The fitted peak positions exhibit a linear relationship with alpha particle energies, achieving a relative energy resolution better than 1 %. To derive the ^{222}Rn time evolution in Figure 4, events within a $\pm 3\,\sigma$ region around the ^{222}Rn peak were selected. The resulting data was corrected for this selection efficiency and dead-time effects. Approximately one-day time bins were chosen to ensure adequate statistics within each bin.

Comparing the two analyses, a 1 % difference was observed during the *No RRS* and the *GXe-only RRS* mode, while a 14 % difference was noted for the *GXe+LXe RRS* mode. To account for these differences, the final ^{222}Rn activity concentration values in each mode were determined as the average of the mean ^{222}Rn activity concentration derived from both analyses. Additionally, half of the difference between Analysis-I and -II was added to the systematic uncertainty (0.01 μBq kg^{-1} for the *No RRS* and *GXe-only RRS* as well as 0.06 μBq kg^{-1} for the *GXe+LXe RRS* mode). The resulting ^{222}Rn activity concentration time evolution was fitted using the model described in section V D.

Detector calibrations conducted prior to the presented time period labeled as *No RRS* in this work were excluded from the analysis to prevent potential bias in the ^{222}Rn activity concentration estimate. Due to this exclusion, the available dataset is limited to a few days only, resulting in a comparatively large statistical uncertainty for the *No RRS* equilibrium value. During the transition from *GXe-only RRS* to *GXe+LXe RRS* mode, further detector calibrations were undertaken. Additionally, the RRS underwent improvements, including a new LXe outlet valve plug and the replacement of gasket material in all piston pumps with Ultra-high molecular weight polyethylene (UHMWPE) to enhance operational stability and xenon purity. These interventions resulted in periods of no or unstable data acquisition (gray shaded period in Figure 4), leading to a lack of data for the initial stages of the *GXe+LXe RRS* mode. Consequently, the available data reflects the system's behavior after radon emanation and removal had reached equilibrium.

C. Radon Source Distribution

The contribution of radon sources within XENONnT originating from the different subsystems varies across different radon removal modes (see Figure 2). The Figure 8 provides a comprehensive overview of these sources and their classifications.

Pure type 1a sources enter directly the LXe in the detector and include the cryostat housing the TPC, the TPC itself, and the GXe-PUR system. These sources are combined into the source term A_{I}. The CRY system, on the other hand, is a pure type 1b source (A_{III}), where radon emanates into the GXe above the detector and can be extracted and guided to the RRS with a high efficiency ϵ_{1b} before migrating into the liquid. Type 2 sources are located upstream of the RRS, and can be almost completely removed before they reach the detector. The classification of the LXe-PUR system (A_{II}) depends on the radon removal mode: In the *No RRS* and *GXe-only RRS* modes, it acts as a pure type

1a source. In the *GXe+LXe RRS* mode, a fraction $\xi \approx 0.2$ of the total LXe flow is diverted to the RRS and becomes a type 2 source. The remaining fraction $(1-\xi)$ is directly entering the detector and is of type 1a. The RRS system itself contributes radon only when actively in use. Across both modes, components upstream of the distillation column (e.g., the GXe Pump and GXe Purifier) are categorized as type 2 (A_V) since the emanated radon enters directly the distillation tower, while components downstream (e.g., Compressor) are type 1a (A_{IV}), as the radon is emanated into the xenon flow after the radon removal process in the distillation tower.

The Figure 8 highlights the dominance of type 1 sources in XENONnT, with type 2 sources being minimal. Type 1a and type 1b sources each constitute approximately 50 % of the total radon contribution. The final ^{222}Rn activity concentration within the TPC is influenced by the RRS's efficiency in reducing these initial sources.
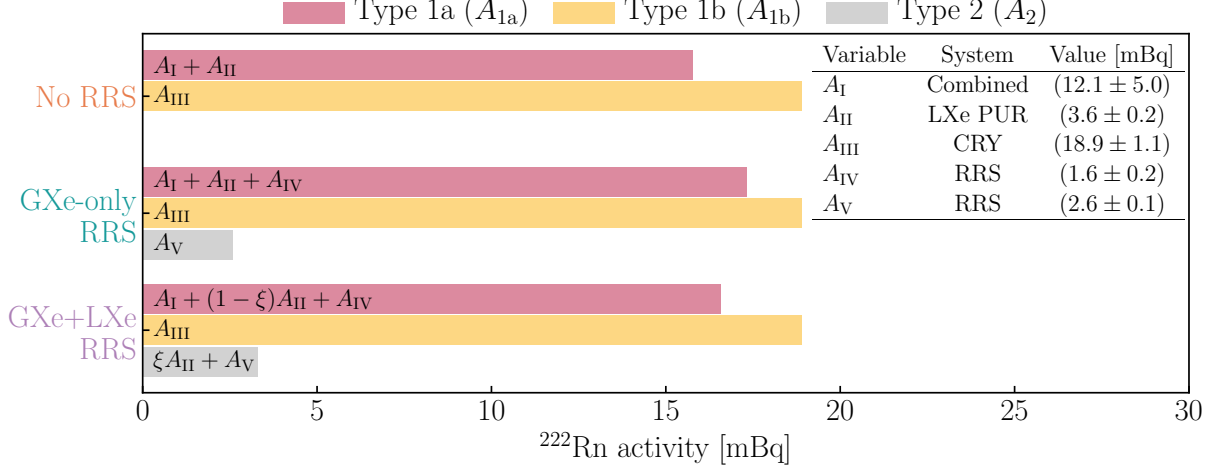

FIG. 8. Radon source distribution in XENONnT prior to radon reduction [25, 27]. Radon source terms are categorized as type 1a (A_{1a}, red), type 1b (A_{1b}, yellow), and type 2 (A_2, gray) varying across the three operational modes. The type 1a sources Cryostat (1.9 ± 0.2), TPC (8.3 ± 5.0) and GXe-PUR (1.9 ± 0.2) are combined into term A_I due to model limitations. The RRS contributes to both type 1a (A_{IV}) and type 2 (A_V) sources when in operation. The LXe fraction ξ diverted from the LXe-PUR to the RRS during the *GXe+LXe RRS* mode is set to the design value $\xi = 0.2$. Note that the RRS's efficiency in reducing the initial radon sources shown here determines the final ^{222}Rn activity concentration within the TPC.

D. Radon Removal Model

A piecewise continuous function, partitioned according to the three operational modes, was employed to model the data in Figure 4. During the *No RRS* period, the ^{222}Rn emanation and decay were in equilibrium, resulting in a constant activity concentration, $a_{\text{No-RRS}}^{\text{eq}}$, given by

$$a_{\text{No-RRS}}^{\text{eq}} = \frac{A_{1a} + A_{1b}}{m_{\text{Xe}}}, \tag{2}$$

where m_{Xe} is the xenon mass in the cryostat, and A_{1a}, A_{1b} represent type 1a and 1b sources (as defined in Figure 8). Type 2 sources do not contribute during this period ($A_2 = 0$).

A time-dependent function describing the ^{222}Rn evolution within the detector's LXe volume during the *GXe-only RRS* or the full *GXe+LXe RRS* mode was developed in Ref. [28]. This function considers both radon inflow (via emanation or remnant ^{222}Rn that was not fully removed by the RRS) and outflow (via extraction and removal, or decay).

Following Ref. [28], the activity concentration, $a_{\mathrm{RRS}}(t)$, for this mode is given by

$$a_{\mathrm{RRS}}(t) = \frac{K}{m_{\mathrm{Xe}}}\frac{\lambda_{\mathrm{Rn}}}{\Lambda} + \left(a_{\mathrm{RRS}}(0) - \frac{K}{m_{\mathrm{Xe}}}\frac{\lambda_{\mathrm{Rn}}}{\Lambda}\right) \cdot e^{-\Lambda \cdot t}, \tag{3}$$

with

$$K = A_{1\mathrm{a}} + (1 - \epsilon_{1\mathrm{b}})A_{1\mathrm{b}} + \frac{A_2 + \epsilon_{1\mathrm{b}}A_{1\mathrm{b}}}{R_{\mathrm{RRS}}}, \tag{4}$$

$$\Lambda = \left(\lambda_{\mathrm{Rn}} + \frac{F_{\mathrm{RRS}}}{m_{\mathrm{Xe}}}\left(1 - \frac{1}{R_{\mathrm{RRS}}}\right)\right), \tag{5}$$

where $\lambda_{\mathrm{Rn}} = 0.18\,\mathrm{d}^{-1}$ is the ^{222}Rn decay constant, $a_{\mathrm{RRS}}(0)$ is the initial activity concentration at the start of the mode, and $\epsilon_{1\mathrm{b}}$ is the efficiency of extracting type 1b sources from the CRY system. The ratio of the RRS process flow F_{RRS} and the xenon mass m_{Xe} characterizes the RRS purification timescale. The RRS reduction factor R_{RRS}, defined as the inlet-to-outlet radon concentration ratio, is assumed constant and independent from the radon concentration.

For long enough times ($t \cdot \Lambda \gg 1$), equilibrium is reached and the second term of Equation 3 vanishes, leading to $a_{\mathrm{RRS}}(\infty) = K/m_{\mathrm{Xe}} \cdot \lambda_{\mathrm{Rn}}/\Lambda$ for the *GXe+LXe RRS* mode. During the *GXe-only RRS* mode, LXe extraction is not active ($F_{\mathrm{RRS}} = 0$). The activity concentration is then described by Equation 3 with $\Lambda = \lambda_{\mathrm{Rn}}$, and the equilibrium plateaus at $a_{\mathrm{RRS}}(\infty) = K/m_{\mathrm{Xe}}$. Please note the different source terms $A_{1\mathrm{a}}, A_{1\mathrm{b}},$ and A_2 in K for both modes as defined in Figure 8.

A χ^2-fit was performed to determine model parameters with the following constraints: ^{222}Rn source terms A_{I} to A_{V} as defined in Figure 8, xenon mass $m_{\mathrm{Xe}} = (8520 \pm 85)\,\mathrm{kg}$ and RRS process flow $F_{\mathrm{RRS}} = (62 \pm 6)\,\mathrm{kg\,h}^{-1}$. The RRS reduction factor R_{RRS} and the extraction efficiency $\epsilon_{1\mathrm{b}}$ were free parameters. The best-fit yielded $\epsilon_{1\mathrm{b}} = (0.88 \pm 0.06)$, and a lower limit for R_{RRS} of > 187 (90 % C.L.). Given the dominant role of the process flow F_{RRS} in the removal efficiency [28], the model exhibits limited sensitivity to large R_{RRS} values, necessitating a one-sided confidence interval.

^{222}Rn reduction factors in the detector for the *GXe-only RRS* ($r_{\mathrm{GXe\text{-}only}}$) and *GXe+LXe RRS* ($r_{\mathrm{GXe+LXe}}$) modes as shown in Figure 4 were determined by comparing the plateau activity concentrations to the initial *No RRS* plateau.

E. Equivalent Solar Neutrino-induced Rate

In order to demonstrate the impact of the radon reduction technique on solar neutrino measurements, the expected solar neutrino rate was converted into an equivalent ^{222}Rn activity concentration. This denotes the ^{222}Rn concentration, at which the rate of ^{214}Pb beta decays matches the expected rate of solar neturino-induced electronic recoils within the energy interval of [5, 30] keV. The rates were computed using two models for the weak neutrino-electron interaction in LXe: A free electron approximation including the stepping of atomic shells (FEA) [50] and an ab initio many-body method, the relativistic random phase approximation (RRPA) [50]. The RRPA model predicts a 23 % lower rate due to atomic binding effects.

The corresponding rate of ^{214}Pb beta decays within [5, 30] keV, required for the conversion from ER event rate to ^{222}Rn activity concentration, cannot be predicted a priori as it depends on detector specific effects. This is because ionized radon progenies from the ^{222}Rn decay chain may partly plate out on the cathode and detector walls under the influence of the electric field and due to LXe convection [31]. This results in reduced concentrations in the LXe bulk for isotopes further down the decay chain. This effect can be seen for the XENONnT data in Figure 3, where the contribution of ^{214}Po is diminished to approximately 40 %. To estimate the ratio between the low-energy beta decays of ^{214}Pb to the activity concentration of ^{222}Rn, XENONnT conducted a dedicated calibration using a ^{222}Rn source [51]. The low energy ER spectrum in this data set is dominated by the ^{214}Pb beta decays, rendering all other contributions from ^{85}Kr, ^{136}Xe or solar neutrinos negligible. Note that this ratio is specific for XENONnT. The resulting equivalent ^{222}Rn activity concentrations, expressed in $\mu\mathrm{Bq\,kg}^{-1}$, are shown as a yellow band in Figure 5, with the upper and lower limits determined by the FEA and RRPA models, respectively.

Different experiments feature different plate-out effects, leading to a different equivalent solar neutrino-induced rate: Assuming a ^{214}Po/^{222}Rn ratio of 20 % and adopting the RRPA model, the equivalent solar neutrino rate is estimated to be $2.2\,\mu\mathrm{Bq\,kg}^{-1}$. A plate-out ratio of 60 % would result in a rate of $0.7\,\mu\mathrm{Bq\,kg}^{-1}$. This range encompasses the values reported for experiments shown in Figure 5, but is omitted for clarity.

ACKNOWLEDGMENTS

---

[1] E. Aprile *et al.* (XENON), "The XENONnT dark matter experiment," Eur. Phys. J. **C84**, 784 (2024), arXiv:2402.10446 [physics.ins-det].

[2] E. Aprile *et al.* (XENON), "First Dark Matter Search with Nuclear Recoils from the XENONnT Experiment," Phys. Rev. Lett. **131**, 041003 (2023), arXiv:2303.14729 [hep-ex].

[3] E. Aprile *et al.* (XENON), "Search for New Physics in Electronic Recoil Data from XENONnT," Phys. Rev. Lett. **129**, 161805 (2022), arXiv:2207.11330 [hep-ex].

[4] D.S. Akerib *et al.*, "The LUX-ZEPLIN (LZ) experiment," Nuclear Instruments and Methods in Physics Research Section A: Accelerators, Spectrometers, Detectors and Associated Equipment **953**, 163047 (2020).

[5] J. Aalbers *et al.*, "First Dark Matter Search Results from the LUX-ZEPLIN (LZ) Experiment," Phys. Rev. Lett. **131**, 041002 (2023).

[6] Yue Meng *et al.*, "Dark Matter Search Results from the PandaX-4T Commissioning Run," Phys. Rev. Lett. **127**, 261802 (2021).

[7] P. Agnes *et al.*, "DarkSide-50 532-day dark matter search with low-radioactivity argon," Phys. Rev. D **98**, 102006 (2018).

[8] Gianfranco Bertone, Dan Hooper, and Joseph Silk, "Particle dark matter: evidence, candidates and constraints," Physics Reports **405**, 279–390 (2005).

[9] Leszek Roszkowski, Enrico Maria Sessolo, and Sebastian Trojanowski, "WIMP dark matter candidates and searches - current status and future prospects," Reports on Progress in Physics **81**, 066201 (2018).

[10] E. Aprile *et al.* (XENON), "Design and performance of the XENON10 dark matter experiment," Astroparticle Physics **34**, 679–698 (2011).

[11] E. Aprile *et al.*, "The XENON100 dark matter experiment," Astroparticle Physics **35**, 573–590 (2012).

[12] E. Aprile *et al.* (XENON), "The XENON1T dark matter experiment," Eur. Phys. J. **C77**, 881 (2017), arXiv:1708.07051 [astro-ph.IM].

[13] G.J. Alner *et al.*, "First limits on WIMP nuclear recoil signals in ZEPLIN-II: A two-phase xenon detector for dark matter detection," Astroparticle Physics **28**, 287–302 (2007).

[14] D.Yu. Akimov *et al.*, "The ZEPLIN-III dark matter detector: Instrument design, manufacture and commissioning," Astroparticle Physics **27**, 46–60 (2007).

[15] D.S. Akerib *et al.*, "The Large Underground Xenon (LUX) experiment," Nuclear Instruments and Methods in Physics Research Section A: Accelerators, Spectrometers, Detectors and Associated Equipment **704**, 111–126 (2013).

[16] C.E Aalseth *et al.*, "DarkSide-20k: a 20 Tonne two-phase LAr TPC for direct dark matter detection at LNGS," Eur. Phys. J. Plus **133**, 131 (2018).

[17] Matteo Agostini *et al.*, "Toward the discovery of matter creation with neutrinoless $\beta\beta$ decay," Rev. Mod. Phys. **95**, 025002 (2023).

[18] M Auger *et al.*, "The EXO-200 detector, part I: detector design and construction," Journal of Instrumentation **7**, P05010 (2012).

[19] G. Adhikari *et al.*, "nEXO: neutrinoless double beta decay search beyond 10^{28} year half-life sensitivity," Journal of Physics G: Nuclear and Particle Physics **49**, 015104 (2021).

[20] E. Aprile *et al.* (XENON), "Observation of two-neutrino double electron capture in ^{124}Xe with XENON1T," Nature **568**, 532–535 (2019), arXiv:1904.11002 [nucl-ex].

[21] E. Aprile *et al.* (XENON), "Double-Weak Decays of ^{124}Xe and ^{136}Xe in the XENON1T and XENONnT Experiments," Phys. Rev. C **106**, 024328 (2022), arXiv:2205.04158 [hep-ex].

[22] E. Aprile *et al.* (XENON), "Removing krypton from xenon by cryogenic distillation to the ppq level," Eur. Phys. J. C **77**, 275 (2017), arXiv:1612.04284 [physics.ins-det].

[23] ENSDF database, "http://www.nndc.bnl.gov/ensarchivals/," (2023).

[24] Ethan Brown *et al.*, "Magnetically-coupled piston pump for high-purity gas applications," Eur. Phys. J. C **78**, 604 (2018), arXiv:1803.08498 [physics.ins-det].

[25] E. Aprile *et al.* (XENON), "^{222}Rn emanation measurements for the XENON1T experiment," Eur. Phys. J. C **81**, 337 (2021), arXiv:2009.13981 [physics.ins-det].

[26] J. Aalbers *et al.*, "A next-generation liquid xenon observatory for dark matter and neutrino physics," J. Phys. G **50**, 013001 (2023), arXiv:2203.02309 [physics.ins-det].

[27] E. Aprile *et al.* (XENON), "Material radiopurity control in the XENONnT experiment," Eur. Phys. J. C **82**, 599 (2022), arXiv:2112.05629 [physics.ins-det].

[28] M. Murra, D. Schulte, C. Huhmann, and C. Weinheimer, "Design, construction and commissioning of a high-flow radon removal system for XENONnT," Eur. Phys. J. C **82**, 1104 (2022), arXiv:2205.11492 [physics.ins-det].

[29] Shaofei Zhu and E.A. McCutchan, "Nuclear Data Sheets for A=214," Nuclear Data Sheets **175**, 1–149 (2021).

[30] J. F. Ziegler, M. D. Ziegler, and J. P. Biersack, "SRIM - The stopping and range of ions in matter (2010)," Nucl. Instrum. Meth. **B268**, 1818 (2010).

[31] E. Aprile *et al.* (XENON100), "Online ^{222}Rn removal by cryogenic distillation in the XENON100 experiment," Eur. Phys. J. **C77**, 358 (2017), arXiv:1702.06942 [physics.ins-det].

[32] J. B. Albert *et al.* (EXO-200 Collaboration), "Investigation of radioactivity-induced backgrounds in EXO-200," Phys. Rev. C **92**, 015503 (2015).

[33] A. Bradley *et al.*, "Radon-related Backgrounds in the LUX Dark Matter Search," Physics Procedia **61**, 658–665 (2015), 13th International Conference on Topics in Astroparticle and Underground Physics, TAUP 2013.

[34] A. Tan *et al.* (PandaX-II Collaboration), "Dark Matter Results from First 98.7 Days of Data from the PandaX-II Experiment," Phys. Rev. Lett. **117**, 121303 (2016).

[35] K. Abe *et al.*, "XMASS detector," Nucl. Instrum. Methods Phys. Res. A **716**, 78–85 (2013).

[36] J. Aalbers *et al.* (The LUX-ZEPLIN Collaboration), "Background determination for the LUX-ZEPLIN dark matter experiment," Phys. Rev. D **108**, 012010 (2023).

[37] Abdusalam Abdukerim *et al.* (PandaX), "PandaX-xT: a Multi-ten-tonne Liquid Xenon Observatory at the China Jinping Underground Laboratory," (2024), arXiv:2402.03596 [hep-ex].

[38] J. Aalbers *et al.* (XLZD), "The XLZD Design Book: Towards the Next-Generation Liquid Xenon Observatory for Dark Matter and Neutrino Physics," (2024), arXiv:2410.17137 [hep-ex].

[39] E. Aprile *et al.* ((XENON Collaboration)¶, XENON), "Offline tagging of radon-induced backgrounds in XENON1T and applicability to other liquid xenon time projection chambers," Phys. Rev. D **110**, 012011 (2024), arXiv:2403.14878 [hep-ex].

[40] J. Aalbers *et al.* (LZ Collaboration), "Dark Matter Search Results from 4.2 Tonne-Years of Exposure of the LUX-ZEPLIN (LZ) Experiment," (2024), arXiv:2410.17036 [hep-ex].

[41] M. Agostini *et al.* (BOREXINO), "Comprehensive measurement of pp-chain solar neutrinos with Borexino," PoS **EPS-HEP2019**, 400 (2020).

[42] E. Aprile *et al.* (XENON), "First Indication of Solar ^{8}B Neutrinos via Coherent Elastic Neutrino-Nucleus Scattering with XENONnT," Phys. Rev. Lett. **133**, 191002 (2024), arXiv:2408.02877 [hep-ex].

[43] Z. Bo *et al.* (PandaX), "First Indication of Solar ^{8}B Neutrino Flux through Coherent Elastic Neutrino-Nucleus Scattering in PandaX-4T," Phys. Rev. Lett. **133**, 191001 (2024), arXiv:2407.10892 [hep-ex].

[44] Ciaran A. J. O'Hare, "New Definition of the Neutrino Floor for Direct Dark Matter Searches," Phys. Rev. Lett. **127**, 251802 (2021).

[45] Eric W. Lemmon, Ian H. Bell, Marcia L. Huber, and Mark O. McLinden, *Thermophysical Properties of Fluid Systems* (NIST Chemistry WebBook, NIST Standard Reference Database Number 69, Eds. P.J. Linstrom and W.G. Mallard, 2024).

[46] M. Murra *et al.*, "Cryogenic bath-type heat exchangers for ultra-pure noble gas applications," JINST **17**, P05037 (2022), arXiv:2203.01026 [physics.ins-det].

[47] D. Schulte *et al.*, "Ultra-clean radon-free four cylinder magnetically-coupled piston pump," JINST **16**, P09011 (2021), arXiv:2107.00755 [physics.ins-det].

[48] E. Aprile *et al.* (XENON), "XENONnT Analysis: Signal Reconstruction, Calibration and Event Selection," Phys. Rev. D **accepted** (2024), arXiv:2409.08778 [hep-ex].

[49] Matteo Guida, *Position Reconstruction Based on Prompt Scintillation Light in XENONnT Exploiting Deep Learning*, Master's thesis, Padua U. (2021).

[50] J.-W. Chen *et al.*, "Low-energy electronic recoil in xenon detectors by solar neutrinos," Physics Letters B **774**, 656–661 (2017).

[51] F. Jörg *et al.*, "Production and characterization of a ^{222}Rn-emanating stainless steel source," Applied Radiation and Isotopes **194**, 110666 (2023).